Chiral plasmonic nanostructures: experimental and numerical tools

Gediminas Gervinskas[a,b], Lorenzo Rosa[a], Etienne Brasselet[c] and Saulius Juodkazis[a,b]

[a] Centre for Micro-Photonics, Faculty of Engineering and Industrial Sciences, Swinburne University of Technology, Hawthorn, Australia;
[b] Melbourne Centre for Nanofabrication, Clayton, Australia;
[c] Université Bordeaux, Laboratoire Ondes et Matière d'Aquitaine, UMR 5798, F-33400 Talence, France and
CNRS, Laboratoire Ondes et Matière d'Aquitaine, UMR 5798, F-33400 Talence, France

ABSTRACT

A combination of electron- and ion-beam lithographies has been applied to fabricate patterns of plasmonic nanoparticles having tailored optical functions: they create hot-spots at predefined locations on the nanoparticle at specific wavelengths and polarizations of the incident light field. Direct inscribing of complex chiral patterns into uniform nano-disks of sub-wavelength dimensions, over extensive 20-by-20 μm^2 areas, is achieved with high fidelity and efficiency; typical groove widths are in 10-30 nm range. Such patterns can perform optical manipulation functions like nano-tweezing and chiral sorting. Fabrication procedures can be optimized to pattern thin 0.1-2.5 μm-thick membranes with chiral nanoparticles having sub-15 nm grooves. Peculiarities of optical force and torque calculations using finite-difference time-domain method are presented.

Keywords: Plasmonics, opto-mechanics, chirality, ion-beam lithography, electron-beam lithography, super-resolution

1. INTRODUCTION

A puzzling and interesting fact that bio-active molecules are left-handed needs to be better understood. In the fields of sensing, medical, and pharmaceutical applications, searching for the fast and reliable sorting of molecules by chirality is very important practical target. The self-induced back-action (SIBA)[1,2] trapping principles are very promising in this regard. Plasmonic light field enhancement[3] at the edges and grooves are used in SIBA when the proximity of the object to be trapped an the hot-spot trap are creating favorable light field distribution for a positive feedback of trapping. The light enhancement is strongest when the width of the groove or gap is in 1-10 nm size span.[4–7] The gaps of tens-of-nanometers are required to boost THz emission to practical levels and has a promise to deliver practical electrically controlled THz sources.[8] Patterns of such high precision are challenging to fabricate especially on the larger area patterns required for efficient trapping, sorting, and even THz applications. Also, precise control and positioning of nanoparticles in random patterns for light harvesting and sensing[9–12] needs high precision of fabrication. Light-driven nano-motors is another new opening in plasmonic applications exploring an inherently chiral light-matter interaction.[13]

On the nanoscale, mechanical manipulation of light and nano-objects of 1-100 nm in cross section is now a frontier research.[13–19] Opto-manipulation of nano-objects and single molecules opens new functionalities in surface enhanced Raman scattering (SERS),[17,19] a new predicted phenomenon of the *pulling* optical force[15] (recent review[20]), nano-manipulation[18] and super-resolution microscopies.[16,19] Flexibility and versatility of manipulation of light on the scale of its wavelength matured in optical microscopies is now applied to nanoscale using plasmonic metallic nano-particles[21] which allow to concentrate and manipulate light on the required 1-100 nm dimensions for manipulation of nano-objects of comparable size.

Further author information: (Send correspondence to G.G.)
G.G.: E-mail: ggervinskas@swin.edu.au

Advanced Fabrication Technologies for Micro/Nano Optics and Photonics VI, edited by Georg von Freymann, Winston V. Schoenfeld, Raymond C. Rumpf, Proc. of SPIE Vol. 8613, 861304 · © 2013 SPIE
CCC code: 0277-786X/13/$18 · doi: 10.1117/12.2002281

Here, we show first demonstration how combination of ion and electron beam lithographies (IBL and EBL)[22,23] can be used for high precision and resolution (sub-15 nm) fabrication of arbitrary patterns over larger arrays of nanoparticles with high fidelity. Chiral patterns were inscribed and tens-of-nanometers grooves can be made and positioned without errors on a single write field. Modeling of optomechanical effects, the torque and force generation by nanoparticles using FDTD, is described and limitations of the method are analyzed.

2. EXPERIMENTAL

2.1 Fabrication of nanoparticles

A unique combination of ion-beam lithography (with Raith IonLiNE) and electron-beam lithography (with Raith 150-TWO) has been utilized to create chiral plasmonic structures with 15-25 nm wide grooves inscribed onto particles down to a controlled depth.

We used PMMA resist (MicroChem Corp) of 200 nm thickness in the first EBL step. After that magnetron sputtering (AXXIS, Kurt J. Lesker) was used for deposition 40 nm thick gold film on a 3 nm Ti adhesion layer on a glass substrate. Following step was standard lift-off in acetone, which produced arrays of cylindrical gold nanoparticles. Typical diameter of nano-cylinders was 750 nm and cylinder arrays without any additional steps were used for a first step of IBL. Patterns of nanoparticles was then processed by IBL and 20-30 nm grooves were inscribed; sub-15 nm resolution can be reached at low milling current and can be further improved if nanoparticles are thinner. Nanoparticles were structurally analyzed using scanning electron microscopy (SEM).

2.2 Modeling by finite difference time domain method

The optical performance of the fabricated patterns has been modelled numerically by the three dimensional (3D) finite difference time domain (FDTD) method (Lumerical software package), with a total-field scattered-field (TFSF) approach that permits to calculate the wideband cross-section and field enhancement response with a single simulation. Patterned plasmonic nano-particle arrays allow tailoring of light field enhancement in both spectral and spatial domains. Optically exerted force and torque calculations for the nano-tweezers and chiral sorting are discussed through the Lorentz force modeling and Maxwell stress tensor approaches and their peculiarities in FDTD method. In particular, implementation of the divergence and rotor (or curl) in FDTD is shown to be critically important for reliable numerical results.

2.3 Definitions and conventions for the light field

The conventions used reflect the ones commonly employed for a paraxial light beam propagating along the z-axis.[24] If no orbital angular momentum (OAM) is present, the electric field distribution of this beam can be represented in complex vectors for z-positive propagation as

$$\mathcal{E} = \mathbf{E}(x,y)\,\mathrm{e}^{-\mathrm{i}(\omega t - kz)}; \qquad \mathbf{E}(x,y) = E_{+1}\hat{\mathbf{u}}_{+1} + E_{-1}\hat{\mathbf{u}}_{-1} \tag{1}$$

where ω is the angular frequency and k is the wavenumber, and where the slowly varying vector complex amplitude $\mathbf{E}(x,y)$ is decomposed into the complex amplitudes $E_{\pm1}$ of its spin components, characterized by the two possible states of the photon spin number, or helicity, $s = \pm 1$. The two states are paired in the equation by the respective unit vectors

$$\hat{\mathbf{u}}_s = \frac{\hat{\mathbf{u}}_x + \mathrm{i}s\hat{\mathbf{u}}_y}{\sqrt{2}} \tag{2}$$

where $\hat{\mathbf{u}}_x$ and $\hat{\mathbf{u}}_y$ are the unit vectors parallel to the transverse coordinates. Thus, each photon carries a SAM of $s\hbar$, directed along the beam axis (parallel if positive, antiparallel if negative). This relates with the beam polarization handedness in that, as the observation is made against the beam propagation direction, $s = +1$ is associated to LHC polarization and $s = -1$ to RHC for z-positive propagation, while the opposite is true for z-negative propagation.

3. RESULTS

First, we show method for fabrication of 10-30 nm chiral grooves on nanoparticles array with perfect centering of the pattern. Then, issues of FDTD calculations for opto-mechanical force and torque generation are discussed.

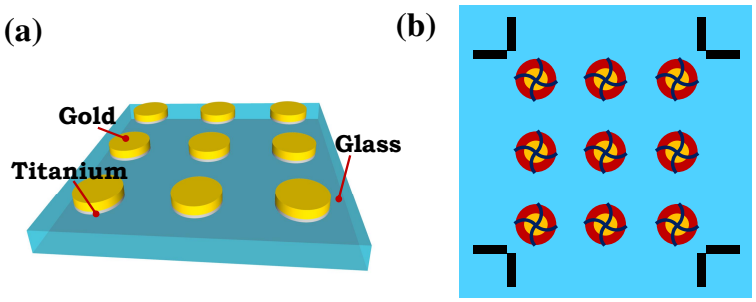

Figure 1. (a) Schematics of the sample: the 40-nm-tall gold cylinders on a 3 nm titanium adhesion layer on a glass substrate. (b) A color-coded manufacturing procedure: first, a write field is manually aligned to the mark tips in the field corners, next, an automatic alignment to the marks is made, then 750 nm diameter gold cylinders are trimmed to the 500 nm diameter, and finally an inscription of arbitrary shaped grooves is performed.

3.1 Fabrication of 20-nm-grooves of arbitrary shape

Standard EBL, metal sputtering and lift-off was applied to fabricate patterns over areas 20×20 μm^2 as required for desk-top laser experiments and SERS under microscope illumination. The nanoparticles were made slightly larger since in the next step concentric trimming by IBL was used to re-define nanoparticles with smaller circumference. This procedure enforce new coordinates and allows for perfect centering of an arbitrary pattern to be inscribed on the nanoparticle. This very same logic can be applied to any shape of nanoparticles with arbitrary shapes of the trimming pattern. If this overlayed trimming is not applied, the positioning error of pattern to be inscribed onto already fabricated particles is ±30 nm in our case and it is too large for high-precision fabrication. This procedure is schematically shown in Fig. 1.

After the concentric trimming was made, chiral patterns were inscribed at low ion current for high precision and resolution patterning. Sub-15 nm wide grooves can be made. This procedure is not time consuming and can be used for practical applications. The resulting array of identical nanoparticles with chiral inscription was obtained (Fig. 2). We assign a handedness to the inscribed chiral shape according to the grooves direction, in particular the particle in Fig. 2 is right-handed, as a supposed right-handed free flow of electrons would couple with the shape to cause "crowding" in the center, possibly originating an enhancement "hot-spot" there. Its mirror image is similarly called left-handed.

3.2 FDTD modeling

The FDTD modeling is carried out on a domain of 1 μm^3, and in first instance the particle is illuminated by a plane wave source shining from the substrate side towards the positive z-direction. Perfectly matched layers are used on the z-axis boundaries, while periodic boundaries conditions are placed on the x- and y-axes. This is necessary to avoid diffraction of the plane wave source at the domain edge, but postulates a periodicity of the structure. This is addressed by enlarging the domain to a wide enough size to distance the periodicized particles and avoid coupling. This in particular was done for the MST calculations, but it greatly increases the time and memory requirements for the model, combined with the requirement to reduce the effect of staircase approximation, which is addressed by reducing the square mesh size around the particle to values smaller than 1 nm (or about $wavelength/1000$), forcing the use of a dedicated machine on a 3D mesh totaling around 2 million grid points. Because of memory limitations, the simulation bandwidth was divided in 500-nm spans, and the simulation time was about 13 hours per span on an 8-core calculation node, with a memory occupancy of about 24 GB.

For the cross-sections calculation, the disk is illuminated by a total-field scattered-field (TFSF) source, which decomposes the total fields in incident fields (known) and scattered fields (unknown), where FDTD remains valid because of Maxwells equations linearity. The region inside the TFSF is solved for the total fields, while the one outside for the scattered fields. The regions are separated by a virtual surface generating the incident wave. If all the structures remain inside the TFSF, there is no incident wave outside, and scattering can be separately assessed. From the known incident power, the absorbed power is calculated. The domain boundary is made of PMLs to avoid scattered field reflection.

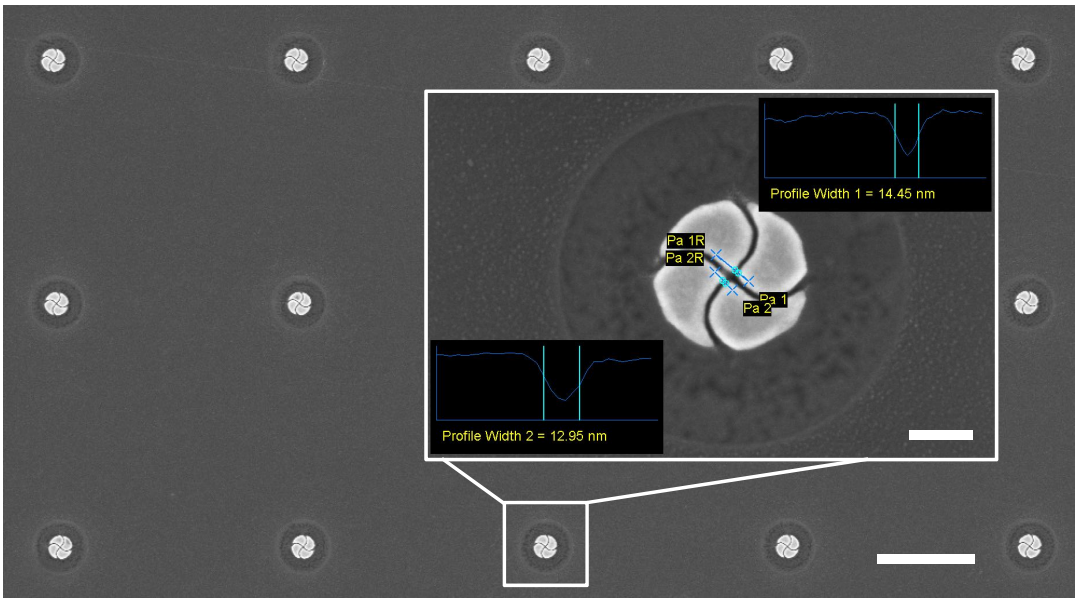

Figure 2. SEM image of a single write-field with fabricated nanoparticles with right-handed chiral signatures inscribed. Inset shows a higher magnification of a single gold cylinder with inscriptions below 15 nm. Scalebars: 2 μm and 200 nm for the inset. The shadow concentric region surrounding the particle is where trimming by ion milling took place.

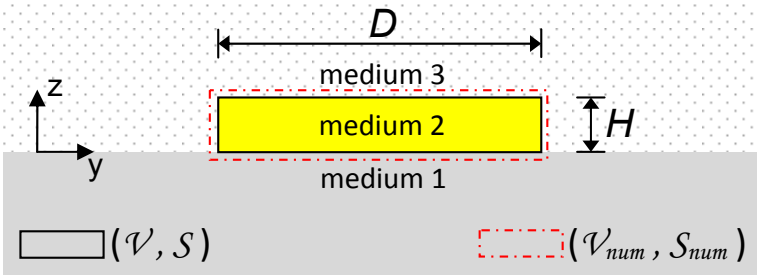

Figure 3. Sketch of the cylindrical nano-particle with diameter D and height H sitting on a SiO_2 substrate and surrounded by air with the definition of the volumes $(\mathcal{V}, \mathcal{V}_{num})$ and associated closed surfaces $(\mathcal{S}, \mathcal{S}_{num})$ involved in the Lorentz and MST evaluation of the total force and torque exerted by light onto the nano-particle.

The results of the simulation on the optical scattering properties of the nano-disk are shown in Fig. 4. The plot depicts the absorption σ_{abs} and scattering σ_{scat} cross-sections (normalized to the geometrical area of the particle). The curves for the achiral disk depicted in Fig. 3 show the narrow-band gold plasmonic resonance at 600 nm wavelength, together with the broad-band particle resonance on glass at 1600 nm (Fig. 4(a)). These properties are independent of the SAM s of the beam. When we consider the chiral particles instead (left-handed in Fig. 4(b) and right-handed in Fig. 4(c)), in particular around the resonant wavelength of 775 nm, we see that illumination with a beam whose spin has the same handedness of the grooves causes the scattering cross-section to increase, and a correspondent decrease in the absorption cross-section, proving the possibility of controlling the optical properties of the particle through the beam momentum.

3.2.1 FDTD calculation of force and torque

We now introduce a general model for calculating forces and torques which takes into account the peculiarities of the 3D finite difference time domain (FDTD) method,[25] in particular using the Lumerical software package. The chiral light-matter interaction is revealed by the FDTD simulations[25] carried out using Lumerical software package. In order to accommodate the finest possible mesh an optimization can be made by using periodic boundary conditions. Fine meshing should be implemented to reveal small spatial fluctuations of the calculated

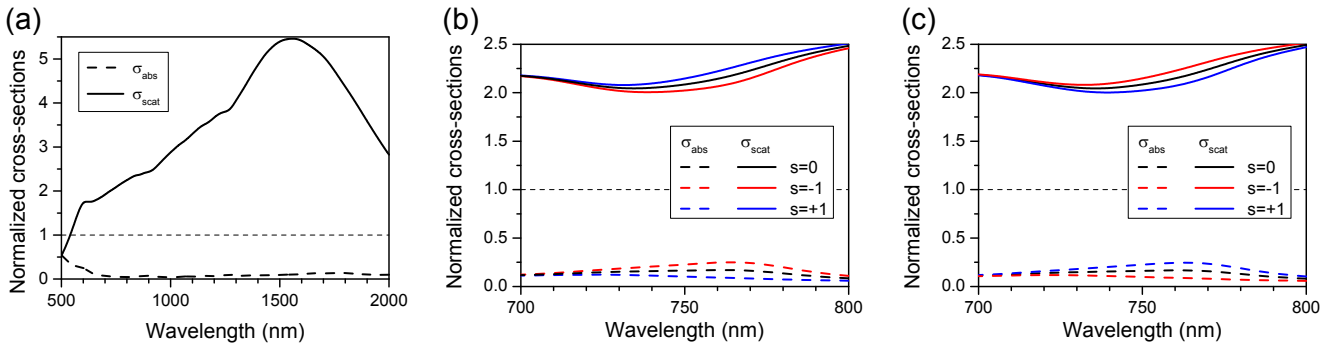

Figure 4. Normalized cross-sections of the 500-nm gold disk on silica, absorption σ_{abs} and scattering σ_{scat}, for (a) (achiral) plain disk, (b) (chiral) left-handed sliced disk, and (c) (chiral) right-handed sliced disk.

fields. The materials are modeled according to the multi-coefficient polynomial approximation of the refractive index values tabulated in the Lumerical database.

Initially, attempts were made to employ conformal meshing to reduce time and memory occupancy without sacrificing accuracy, however it was found that the index monitors used to determine the value of ε for the different frequencies returned the same values as those obtained by staircase meshing. These do not correspond strictly to the permittivities which the fields at the boundaries of different media are calculated for, introducing significant errors in subsequent calculations.

We developed two different mathematical formulations to calculate force and torque: firstly by calculating the Lorentz force contribution due to induced charges and currents in the metal particles[26] and integrating it on the metallic volume sampled by a 3D monitor, and secondly by calculating the Maxwell stress tensor (MST) and integrating it on a closed box composed by six 2D monitors, surrounding the particle.

In the Lorentz force formulation, the simulation is carried out on a domain slightly larger than the particle. The illumination was initially carried out by a plane wave, then we found that this formulation gives better results when illumination is carried out by a total-field scattered-field (TFSF) source shining in the positive z-direction. Perfectly matched layers (PMLs) are laid out on all boundaries to suppress the light scattered by the particle, and the 3D monitor gathers the total field impinging on the particle.

3.2.2 Lorentz force formalism

From the complex E- and H-fields gathered by the 3D monitor, we derive the time-averaged optical force and torque acting on the particle by integrating the Lorentz force per unit volume on the finite cubes belonging to the metal only (Fig. 5). Mass density and the optical constants of the media are assumed to remain constant under internal and external pressures, and material flow and deformation are ignored. Gold is modeled according to the tabulated values in the Lumerical database, whose imaginary part is considered due to the conductivity contribution. We separate the contribution to the radiation pressure of the electrical charge density from that of the current density; in a dielectric they are only due to the "bound" electrons, while in a metal there is a contribution from the "free" electrons as well, and they are accounted for by the conductivity contribution to the imaginary part of the metal permittivity. In the present FDTD formulation, only the free electrons contribute to the divergence of $\mathbf{D}$ (in the following, the complex representative vectors of electromagnetic quantities will be indicated in bold).

Time-harmonic fields are written according to the convention $\mathcal{E}(x,y,z,t) = \mathbf{E}(x,y,z)\exp(-\mathrm{i}\omega t)$, where $\omega = 2\pi f$ is the angular frequency. Therefore, the time-averaged product $\langle C\rangle$ of two fields $\mathbf{A}$ and $\mathbf{B}$ is written $\langle C\rangle = \frac{1}{2}\mathrm{Re}(\mathbf{A}\mathbf{B}^*)$.

Once the monitor returns the $\mathbf{E}$ and $\mathbf{H}$ fields, we calculate $\mathbf{B} = \mu_0\mathbf{H}$, and (supposing linear media) $\mathbf{D} = \varepsilon_0\varepsilon_r\mathbf{E} = \varepsilon_0\mathbf{E}+\mathbf{P}$, where $\mathbf{P}$ is the material polarization due to the bound charges and ε_r is complex if the medium is not transparent. At the interface between metal and dielectric, the component of $\mathbf{E}$ parallel to the interface is continuous. The component of $\mathbf{D}$ perpendicular to the interface must also be continuous, which means the

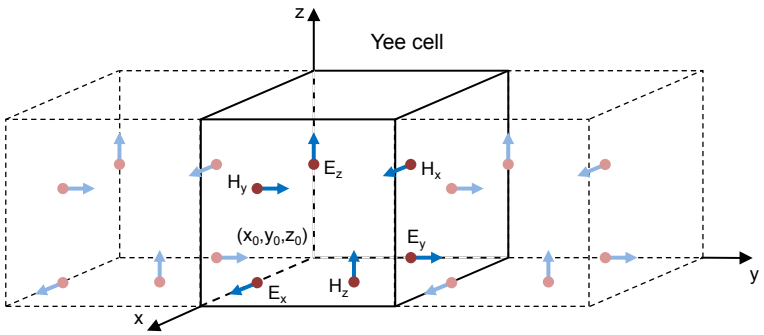

Figure 5. Row of cubic Yee cells forming the 3D-FDTD mesh. The cell origin is in (x_0, y_0, z_0) and the orientations and positions of the six calculated field components are indicated.

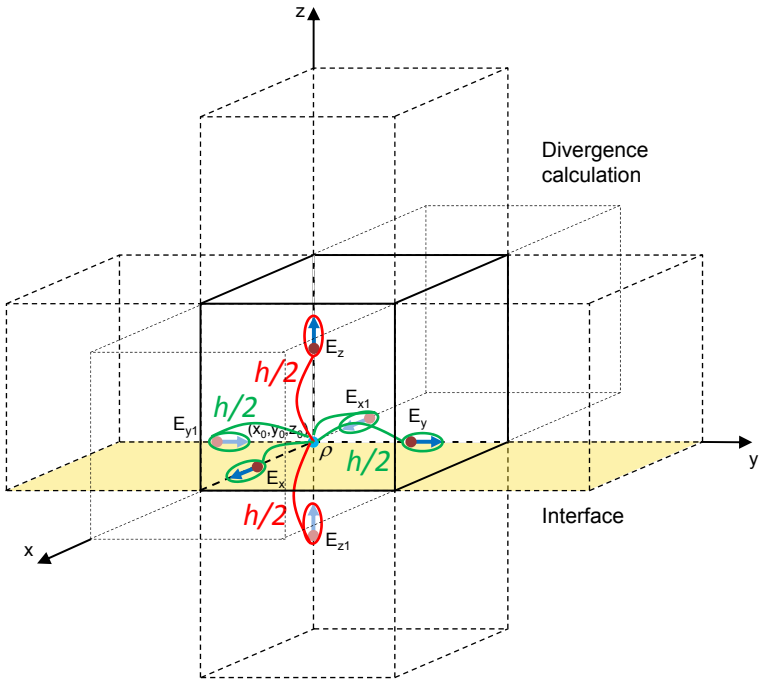

Figure 6. Supposing the interface to run along the xy-plane passing through the origin (x_0, y_0, z_0), the backward differences method is used to calculate $\rho = \varepsilon_0 \nabla \cdot \mathbf{E}$. The red curves indicate finite differences of components discontinuous at the interface, while the green curves indicate differences of interface-continuous ones.

perpendicular component of $\mathbf{E}$ must be discontinuous and originate a charge density $\rho = \rho_b + \rho_f$ on the surface of the object, where ρ_b is the bound charge and ρ_f is the free charge. Since by definition $\rho_b = -\nabla \cdot \mathbf{P}$ and $\rho_f = \nabla \cdot \mathbf{D}$

$$\rho = \varepsilon_0 \nabla \cdot \mathbf{E}. \tag{3}$$

The calculation of charge density ρ through the divergence of the electric field must take into account an unavoidable feature of the FDTD method in that each field component (E_x, E_y, E_z, H_x, H_y, H_z) is calculated in a different point of the Yee cell, as shown in Fig. 5. This is compounded with the fact that, while the component of the electric field parallel to the metal interface is continuous, the perpendicular component is discontinuous and, while for flat interfaces this is straightforward, on curved surfaces the staircase effect given by the FDTD mesh makes the operation ambiguous.

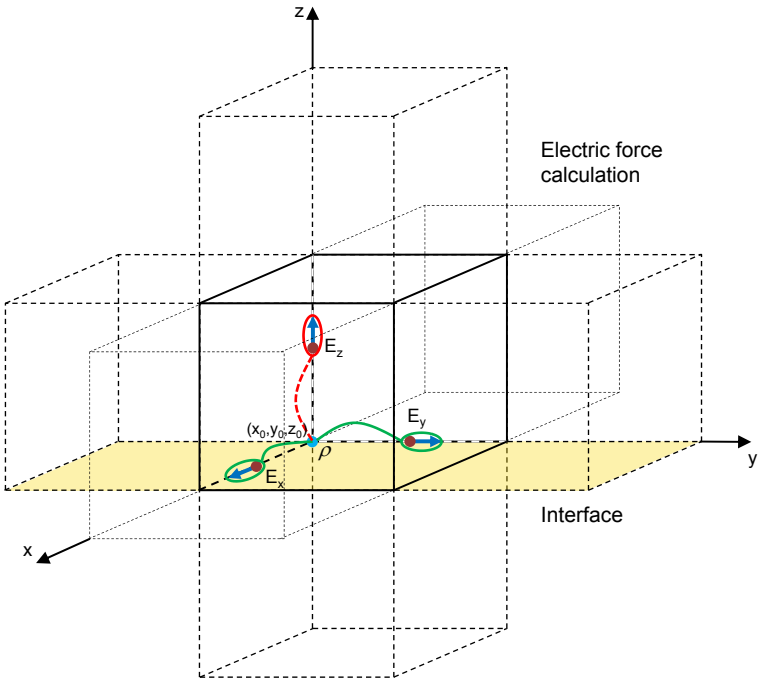

Figure 7. The electric field components are interpolated to the origin (x_0, y_0, z_0) where ρ is defined, to calculate the electric force. Using the same color code as Fig. 6, but this time referring to the interpolation procedure, the dashed curve indicates the interpolation of E_z towards its discontinuity.

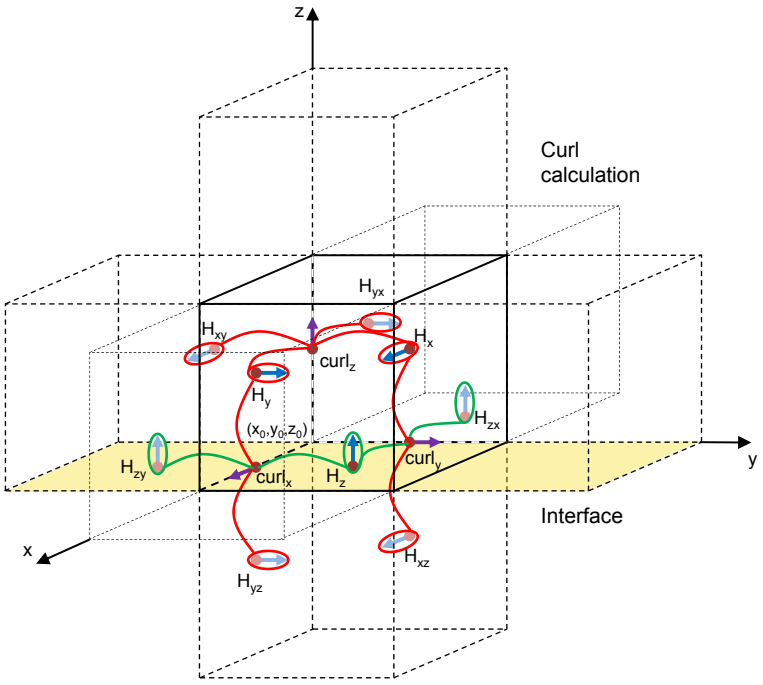

Figure 8. In the same configuration as before, the backward differences method is used to calculate $\nabla \times \mathbf{H} = (curl_x, curl_y, curl_z)$. Using the same color code as Fig. 6, the three components of the curl are calculated in the positions associated with the E-field components they will be summed up with to calculate the magnetic force.

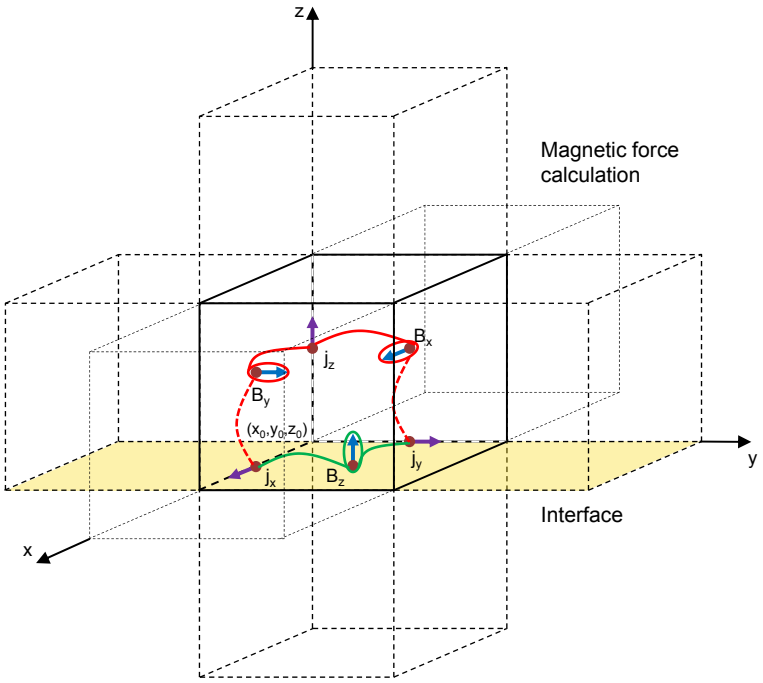

Figure 9. The magnetic induction field components are interpolated to the positions where **j** is defined, to calculate the magnetic force. Using the same color code as Fig. 7, the dashed curves indicate the interpolation of B_x and B_y towards their discontinuity.

This is usually addressed by interpolating all field components back to a common set of (x_0, y_0, z_0) cell origin points, however in the case of components discontinuous at the interface (such as, in this case, E_z, H_x, and H_y), the interpolation error can be not negligible even with a detailed mesh. In fact, interpolating near a discontinuity typically makes the electric field just inside the metal much larger than it really is, especially when the electric field component normal to the metal surface is large.[25] With this in mind, due to the positioning of the electric field components inside the cell, the natural differentiation method for calculating the discrete divergence without interpolations, shown in Fig. 6, gives the value of ρ in (x_0, y_0, z_0) from the values E_x, E_y, and E_z in the current cell, and the values in the cells one mesh step behind the current one. This is known as the backward differences method:

$$\begin{aligned} \nabla \cdot \mathbf{E}(x,y,z) &= \frac{E_x(x,y,z) - E_x(x-h,y,z)}{h} \\ &+ \frac{E_y(x,y,z) - E_y(x,y-h,z)}{h} \\ &+ \frac{E_z(x,y,z) - E_z(x,y,z-h)}{h}, \end{aligned} \tag{4}$$

supposing cubic elements of size h in all directions. Under the influence of the local field, the induced charges give rise to an electric Lorentz force per unit volume

$$\langle \mathbf{f}_e \rangle = \frac{1}{2}\mathrm{Re}(\rho \mathbf{E}^*). \tag{5}$$

In order to compute the three force components, an interpolation choice must be taken, which is to interpolate E_x, E_y, and E_z in (x_0, y_0, z_0), as shown in Fig. 7. As E_z is discontinuous in (x_0, y_0, z_0), the interpolation procedure will result in its average value across the boundary, which will affect the z-component of the electric

force. However, according to Mansuripur,[26] this is physically correct as it eliminates the local perpendicular E-field produced by the interfacial charges from the total field, as the charge cannot exert a force on itself.

The second force term is originated by the interaction of the field with the surface current density $\mathbf{j} = \mathbf{j}_b + \mathbf{j}_f$, where $\mathbf{j}_b$ is due to the bound charge and $\mathbf{j}_f$ is due to the free charge.

From the Maxwell's equations we have $\mathbf{j}_f = \nabla \times \mathbf{H} - \varepsilon_0 \varepsilon_r \frac{\partial \mathbf{E}}{\partial t}$ or, in time-harmonic terms, $\mathbf{j}_f = \nabla \times \mathbf{H} + \mathrm{i}\omega\varepsilon_0\varepsilon_r \mathbf{E}$, which gives

$$\mathbf{j} = \nabla \times \mathbf{H} + \mathrm{i}\omega\varepsilon_0 \mathbf{E}. \tag{6}$$

Similarly as before, the curl operation has been implemented by using the backward differences method, choosing the difference scheme detailed in Fig. 8, which simultaneously avoids interpolations and gives the curl components in the positions where the E-field components are known, making the calculation of $\mathbf{j}_f$ straightforward. For example, the component $curl_z$ is calculated from H_x and H_y in the current cell, H_{xy} in the cell one step behind in the y-direction, and H_{yx} in the cell one step behind in the x-direction. The other components are similarly calculated; the method can thus be represented as:

$$\begin{aligned}
\nabla \times \mathbf{H}(x,y,z) \;=\; & \left[\frac{H_z(x,y,z) - H_z(x,y-h,z)}{h} \right. \\
- \; & \left. \frac{H_y(x,y,z) - H_y(x,y,z-h)}{h} \right] \hat{\mathbf{u}}_x \\
+ \; & \left[\frac{H_x(x,y,z) - H_x(x,y,z-h)}{h} \right. \\
- \; & \left. \frac{H_z(x,y,z) - H_z(x-h,y,z)}{h} \right] \hat{\mathbf{u}}_y \\
+ \; & \left[\frac{H_y(x,y,z) - H_y(x-h,y,z)}{h} \right. \\
- \; & \left. \frac{H_x(x,y,z) - H_x(x,y-h,z)}{h} \right] \hat{\mathbf{u}}_z .
\end{aligned} \tag{7}$$

The H-field then exerts a force on the current density according to the Lorentz law, that is

$$\langle \mathbf{f}_h \rangle = \frac{1}{2} \mathrm{Re}(\mathbf{j} \times \mathbf{B}^*). \tag{8}$$

The cross product calculation requires once again a choice of the interpolation procedure, in this case to interpolate the $\mathbf{B}$ vector component in the positions where the components of $\mathbf{j}$ are defined, as shown in Fig. 9. In this case, both B_x and B_y are discontinuous at the interface, however with this scheme the interpolation error only affects $\langle f_{hz} \rangle = \frac{1}{2}\mathrm{Re}(j_x B_y^* - j_y B_x^*)$; due to this, its effect can be estimated, as will be shown at the end of this discussion. The three components of the magnetic force are then interpolated again to (x_0, y_0, z_0) in order to be summed up with the electric force ones. The total force per unit volume $\langle \mathbf{f} \rangle = \langle \mathbf{f}_e \rangle + \langle \mathbf{f}_h \rangle$ is then integrated on the metal volume $\mathcal{V}$, as depicted in Fig. 3, obtaining

$$\mathbf{F} = \iiint_{\mathcal{V}} \langle \mathbf{f} \rangle \, \mathrm{d}v. \tag{9}$$

The total torque $\mathbf{\Gamma} = \iiint_{\mathcal{V}} \mathbf{r} \times \langle \mathbf{f} \rangle \, \mathrm{d}v$, where $\mathbf{r} = (x, y, z)$, is similarly calculated.

Regarding the interpolation error on $\langle f_{hz} \rangle$, one can immediately see that it does not impact the calculation of Γ_z; moreover, given the asymmetrical positioning of the magnetic field components inside the Yee cell as shown in Fig. 9, it will affect differently elements positioned on opposite metal edges, even in a symmetrical structure. If relevant, this will directly impact the calculation of Γ_x and Γ_y, giving non-zero values for symmetrical structures, which can then be directly assumed as the error bounds of the simulation.

3.2.3 Maxwell stress tensor formalism

Once the electromagnetic field has been calculated, the time-averaged optical force and torque exerted on the gold nano-particle are derived from the MST $\langle \mathbb{T} \rangle$, where $\langle\ \rangle$ denotes time-averaging over an optical cycle. Its elements in the Cartesian coordinate system (x, y, z) with unit vectors $(\hat{\mathbf{u}}_x, \hat{\mathbf{u}}_y, \hat{\mathbf{u}}_z)$ are

$$\langle \mathbb{T} \rangle_{ij} = \frac{1}{2} \mathrm{Re} \left[E_i D_j^* + H_i B_j^* - \frac{1}{2} \left(\mathbf{E} \cdot \mathbf{D}^* + \mathbf{B} \cdot \mathbf{H}^* \right) \delta_{ij} \right] , \tag{10}$$

where δ_{ij} is the Kronecker symbol and $\mathbf{E}$, $\mathbf{D}$, $\mathbf{B}$ and $\mathbf{H}$ are the complex representative vectors for electric, displacement, magnetic induction and magnetic fields, respectively. Re and * refer to real part and complex conjugate, respectively. The optical force volume density (in $\mathrm{N{\cdot}m^{-3}}$ units) is given by the divergence of the MST

$$\mathbf{f}^v = \boldsymbol{\nabla} \cdot \langle \mathbb{T} \rangle . \tag{11}$$

The force $\mathbf{F}$ and torque $\boldsymbol{\Gamma}$ exerted by light on a nano-particle is therefore calculated by using the divergence theorem. In practice we use

$$\mathbf{F} = \iint_{\mathcal{S}_{\mathrm{num}}} \langle \mathbb{T} \rangle \cdot \hat{\mathbf{n}}_{\mathrm{ext}}\ ds \quad \text{and} \quad \boldsymbol{\Gamma} = \iint_{\mathcal{S}_{\mathrm{num}}} \mathbf{r} \times \left(\langle \mathbb{T} \rangle \cdot \hat{\mathbf{n}}_{\mathrm{ext}} \right) ds \tag{12}$$

where, numerically, $\mathcal{S}_{\mathrm{num}}$ is the closed-box surrounding surface located at a distance of 10 nm from the nano-particle interface $\mathcal{S}$, as depicted in Fig. 3, and $\hat{\mathbf{n}}_{\mathrm{ext}}$ is the outward unit vector normal to that surface. This value is chosen to avoid the effect of the sharp electric field discontinuity at the metal-dielectric interface, considering that, as the FDTD method calculates each field component in a different position within the elementary cube, all components are interpolated back to the center of each cube. As metal-dielectric interfaces have a strong discontinuity in the normal E-field component, the interpolation error tends to overestimate the field amplitude close to the interface. At a distance of 10 mesh layers or more, the effect becomes negligible. The interpolation points are kept constant by fixing the mesh position in the neighborhood of the nano-particle.

4. DISCUSSION

Laser trapping and manipulation of birefringent and chiral objects is expected to benefit from use of chiral nanoparticles.[16,27–34] Femtosecond laser fabrication of micro-optical structures which can transform angular momentum of light are expected to add new functionalities in micro-fluidics and sorting.[35–40] Plasmonic sensing[41–44] will benefit from the demonstrated capability to control chirality of nanoparticles on nanoscale.

Uniform patterning with 15-25 nm (at FWHM) grooves is demonstrated here on $20 \times 20\ \mu\mathrm{m}^2$ areas by utilizing the IBL direct-write technique can be used as the final step after membranes are formed. The shown processing steps for reliable fabrication of nanoparticles can be, in principle, complimented by further fabrication steps from the back-side of a sample to make membranes. For example plasma or chemical etching with proper sealing of the front side with nanoparticles is feasible. For optical trapping transparent membranes with nanoparticles is a promising platform.[45,46] The flexibility, thermal conductivity and optical transmission of the membrane allows to explore integration of such samples into opto-fluidic and optical-MEMS structures. Usual lift-off fabrication of plasmonic nanoparticles on membranes is not possible due to membrane fragility, which is not compatible with ultrasonic bath development during lift-off.

An alternative calculation method for the Lorentz force makes use of the vector manipulation routines of MATLAB, where the vector components of the fields are transferred from Lumerical by using text files. In this regards, special care has to be taken when scanning the 3D matrix indices, as MATLAB stores matrices in the column-major format typical of FORTRAN and related languages (unlike the row-major format employed by the C-family languages). The actual order of index scanning thus depends on the internal representation and axis directions of the FDTD solver; for consistency in the case of Lumerical, we scan the y-axis first, then the x-axis, and the z-axis last. In this case, care must be taken for the calculation of the divergence and curl of the vectors, as MATLAB employs the central differences scheme, where the difference is taken between the values

one mesh step ahead and one mesh step behind the current element. While this usually provides a smoother averaging of quantities on the discrete mesh, for the calculation of $\nabla \cdot \mathbf{E}$ this means that the charge value would be nonzero both inside and outside the metal-dielectric interface. Since this is nonphysical outside the metal, the integration domain for charge must be carefully considered.

The FDTD implementation of the MST formulation suffers several issues, which in the end make the Lorentz force formulation preferable. In particular, there are problems with the monitors which form the integration surface, which in FDTD is necessarily cubic and might be non-conformal to the object studied, and when intersecting other materials would invalidate the results. Also, when the monitor crosses an interface between different materials, the fact that the various components are known in different points around the cell creates interpolation problems difficult to solve, as the interface itself becomes a location of significant contribution to force and torque and also the one suffering from the largest interpolation errors. Moreover, there is a third order of problems related specifically to time-domain methods, in that the simulation should wait for the electromagnetic field in the domain to decay completely, and the distance between the monitors and the objects introduces an additional delay that must be waited for. In case the structure under examination has dispersive properties (i.e. the scattered field components at different wavelengths propagate at different speeds), a particularly nasty issue is introduced, in that the simulation stopping point calculated on the average residual field power inside the domain might be correct for some wavelengths, but too early for others, invalidating parts of the spectra whose extension is unpredictable.

5. CONCLUSIONS

We demonstrate possibility to use ion beam post-fabrication of arrays of nanoparticles with sub-15 nm resolution at high fidelity, i.e., all the nanoparticles have same nano-inscribed features of complex chiral shape; the centering of the nano-inscriptions on a nanoparticles has no error of positioning. This is achieved over entire chosen field of write which can be as large as sub-1 mm in cross section.

We calculated the optical cross-sections of non-chiral and chiral particles, and we showed how the optical response of a chiral particle can be controlled by the momentum of the illuminating beam. We introduced a general model applied to FDTD method for calculating forces and torques with two different approaches, Lorentz force and Maxwell stress tensor, along with implementation methodologies to control possible inherent inaccuracies.

ACKNOWLEDGMENTS

Project was supported by the Australian Research Council DP120102980 grant and concept was developed in DP110101769 (2010) and DP120102905 (2011) applications.

REFERENCES

[1] Yang, A. H. J., Moore, S. D., Schmidt, B. S., Klug, M., Lipson, M., and Erickson, D., "Optical manipulation of nanoparticles and biomolecules in sub-wavelength slot waveguides," *Nature* **457**, 71–75 (2009).
[2] Juan, M. L., Gordon, R., Pang, Y., Eftekhari, F., and Quidant, R., "Self-induced back-action optical trapping of dielectric nanoparticles," *Nat. Physics* **5**, 915 – 919 (2009).
[3] Juan, M. L., Righini, M., and Quidant, R., "Plasmon nano-optical tweezers," *Nature Photonics* **5**, 349 – 356 (2011).
[4] Ueno, K., Juodkazis, S., Mizeikis, V., Sasaki, K., and Misawa, H., "Clusters of closely spaced gold nanoparticles as a source of two-photon photoluminescence at visible wavelengths," *Adv. Mat.* **20**(1), 26 – 29 (2008).
[5] Juodkazis, S., Rosa, L., and Nishijima, Y., [*Nanoplasmonics: advanced device applications*], ch. Plasmonic solutions for light harvesting in solar and sensing applications, CRC Press Tailor and Francis group (2013 (in press; October 15, 2013)).
[6] Kowalska, E., Nishijima, Y., Rosa, L., and Juodkazis, S., [*Silver-gold nano-composites for photo-catalytic and sensing applications*], Nova Book Publishers, New York (2013 (in press)).
[7] Juodkazis, S. and Rosa, L., "Surface defect mediated electron hopping between nanoparticles separated by a nano-gap," *physica status solidi - rapid research letters* **4**(10), 244–246 (2010).
[8] Tanoto, H., Teng, J., Wu, Q., Sun, M., Chen, Z., Maier, S., Wang, B., Chum, C., Si, G., Danner, A., et al., "Greatly enhanced continuous-wave terahertz emission by nano-electrodes in a photoconductive photomixer," *Nature Photonics* **6**(2), 121–126 (2012).

[9] Rosa, L., Sun, K., and Juodkazis, S., "Serpinski fractal plasmonic nanoantennas," *physica status solidi - rapid research letters* **5**(5-6), 175–177 (2011).
[10] Juodkazis, K., Juodkazytė, J., Kalinauskas, P., Jelmakas, E., and Juodkazis, S., "Photoelectrolysis of water: Solar hydrogen - achievements and perspectives," *Opt. Express: energy express* **18**, A147–A160 (2010).
[11] Nishijima, Y., Rosa, L., and Juodkazis, S., "Surface plasmon resonances in periodic and random patterns of gold nano-disks for broadband light harvesting," *Opt. Express* **20**(10), 11466–11477 (2012).
[12] Jayawardhana, S., Rosa, L., Buividas, R., Stoddart, P. R., and Juodkazis, S., "Light enhancement in surface-enhanced Raman scattering at oblique incidence," *Photonic Sensors* **2**(3), 283–288 (2012).
[13] Liu, M., Zentgraf, T., Liu, Y., Bartal, G., and Zhang, X., "Light-driven nanoscale plasmonic motors," *Nat. Nanotechnol.* **5**, 570–573 (July 2010).
[14] Rodríguez-Herrera, O. G., Lara, D., Bliokh, K. Y., Ostrovskaya, E. A., and Dainty, C., "Optical nanoprobing via spin-orbit interaction of light," *Phys. Rev. Lett.* **104**, 253601 (Jun 2010).
[15] Chen, J., Ng, J., Lin, Z., and Chan, C., "Optical pulling force," *Nature Photon.* **5**(9), 531–534 (2011).
[16] Brasselet, E. and Juodkazis, S., "Intangible pointlike tracers for liquid-crystal-based microsensors," *Phys. Rev. A* **82**, 063832 (2010).
[17] Cang, H., Labno, A., Lu, C., Yin, X., Liu, M., Gladden, C., Liu, Y., and Zhang, X., "Probing the electromagnetic field of a 15-nanometre hotspot by single molecule imaging," *Nature* **469**, 385–388 (Jan. 2011).
[18] Tong, L., Miljković, V. D., and Käll, M., "Alignment, rotation, and spinning of single plasmonic nanoparticles and nanowires using polarization dependent optical forces," *Nano Lett.* **10**(1), 268–273 (2010). PMID: 20030391.
[19] Stranahan, S. M. and Willets, K. A., "Super-resolution optical imaging of single-molecule sers hot spots," *Nano Lett.* **10**(9), 3777–3784 (2010).
[20] Dogariu, A., Sukhov, S., and Saenz, J. J., "Optically induced negative forces," DOI: 10.1038/NPHOTON.2013.315 (2013 (published online)).
[21] Maier, S. A., [*Plasmonics: Fundamentals and Applications*], Springer, Berlin, Germany (2007).
[22] Rosa, L., Sun, K., Szymanska, J., Hudson, F. E., Dzurak, A., Linden, A., Bauerdick, S., Peto, L., and Juodkazis, S., "Tailoring spectral position and width of field enhancement by ion-beam trimming of plasmonic nanoparticles," *physica status solidi - rapid research letters* **4**(10), 262 – 264 (2010).
[23] Rosa, L., Sun, K., Mizeikis, V., Bauerdick, S., Peto, L., and Juodkazis, S., "3d-tailored gold nanoparticles for light field enhancement and harvesting over visible-ir spectral range," *J. Chem. Phys. C* **115**, 5251–5256 (2011).
[24] Torres, J. P., Torner, L., and (Eds.), [*Twisted Photons: Applications of Light with Orbital Angular Momentum*], WILEY-VCH Verlag, Weinheim, Germany (2011).
[25] Taflove, A. and Hagness, S. C., [*Computational Electrodynamics: The Finite-Difference Time-Domain Method*], Artech House Publishers, Norwood, MA, 3 ed. (2005).
[26] Mansuripur, M., "Radiation pressure and the linear momentum of the electromagnetic field," *Opt. Express* **12**, 5375–5401 (Nov. 2004).
[27] Brasselet, E. and Juodkazis, S., "Optical Angular Manipulation of Liquid Crystal Droplets in Laser Tweezers," *J. of Nonlin. Opt. Phys. and Mat.* **18**(2), 167–194 (2009).
[28] Brasselet, E., Balčiūnas, T., Murazawa, N., Juodkazis, S., and Misawa, H., "Light-induced nonlinear rotations of nematic liquid crystal droplets trapped in laser tweezers," *Mol. Cryst. Liq. Cryst.* **512**, 1989–1997 (2009).
[29] Brasselet, E., Murazawa, N., Misawa, H., and Juodkazis, S., "Optical vortices from liquid crystal droplets," *Phys. Rev. Lett.* **103**, 103903 (2009).
[30] Brasselet, E., Murazawa, N., Juodkazis, S., and Misawa, H., "Statics and dynamics of radial nematic droplets manipulated by laser tweezers," *Phys. Rev. E* **77**, 041704 (2008).
[31] Juodkazis, S., Shikata, M., Takahashi, T., Matsuo, S., and Misawa, H., "Size dependence of rotation frequency of individual laser trapped liquid crystal droplets," *Jpn. J. Appl. Phys.* **38**, L518–520 (1999).
[32] Juodkazis, S., Mizeikis, V., Matsuo, S., Ueno, K., and Misawa, H., "Three-dimensional micro- and nano-structuring of materials by tightly focused laser radiation," *Bull. Chem. Soc. Jpn.* **81**(4), 411–448 (2008).
[33] Juodkazis, S., Shikata, M., Takahashi, T., Matsuo, S., and Misawa, H., "Fast optical swithing by a laser manipulated microdroplet of liquid crystal," *Appl. Phys. Lett.* **74**(24), 3627–3629 (1999).
[34] Takasone, T., Juodkazis, S., Kawagishi, Y., Yamaguchi, A., Matsuo, S., Sakakibara, H., Nakayama, H., and Misawa, H., "Flexural rigidity of a single microtubule," *Jpn. J. Appl. Phys.* **41**(5A), 3015–3019 (2002).
[35] Brasselet, E., Malinauskas, M., Žukauskas, A., and Juodkazis, S., "Photo-polymerized microscopic vortex beam generators : precise delivery of optical orbital angular momentum," *Appl. Phys. Lett.* **97**, 211108 (2010).
[36] Kondo, T., Juodkazis, S., Mizeikis, V., Matsuo, S., and Misawa, H., "Fabrication of three-dimensional periodic microstructures in photoresist SU-8 by phase-controlled holographic lithography," *New J. Phys.* **8**(10), 250 (2006).
[37] Seet, K. K., Mizeikis, V., Kannari, K., Juodkazis, S., Misawa, H., Tetreault, N., and John, S., "Templating and replication of spiral photonic crystals for silicon photonics," *J. Selec. Topics Quant Electr. (IEEE)* **14**(4), 1064 – 1073 (2008).
[38] Seet, K. K., Mizeikis, V., Matsuo, S., Juodkazis, S., and Misawa, H., "Three-dimensional spiral - architecture photonic crystals obtained by direct laser writing," *Adv. Mat.* **17**(5), 541 – 545 (2005).

[39] Seet, K. K., Juodkazis, S., Jarutis, V., and Misawa, H., "Feature-size reduction of photopolymerized structures by femtosecond optical curing of SU-8," *Appl. Phys. Lett.* **89**, 024106 (2006).
[40] Seet, K. K., Mizeikis, V., Juodkazis, S., and Misawa, H., "Three-dimensional horizontal circular spirals photonic crystals with stop gaps below 1 μm," *Appl. Phys. Lett.* **88**(22), 221101 (2006).
[41] Islam, M. M., Ueno, K., Juodkazis, S., Yokota, Y., and Misawa, H., "Development of interdigitated array electrodes with SERS functionality," *Analytical Sciences* **26**, 13–18 (2010).
[42] Ueno, K., Juodkazis, S., Mizeikis, V., Sasaki, K., and Misawa, H., "Spectrally-resolved atomic-scale variations of gold nanorods," *J. Am. Chem. Soc.* **128**(44), 14226–14227 (2006).
[43] Ueno, K., Juodkazis, S., Mino, M., Mizeikis, V., and Misawa, H., "Spectral sensitivity of uniform arrays of gold nanorods to the dielectric environment," *J. Phys. Chem. C* **111**(11), 4180–4184 (2007).
[44] Ueno, K., Yokota, Y., Juodkazis, S., Mizeikis, V., and Misawa, H., "Nano-structured materials in plasmonics and photonics," *Current Nanoscience (CNANO)* **4**(3), 232–235 (2008).
[45] Juodkazis, S., Nishi, Y., Misawa, H., Mizeikis, V., Schecker, O., Waitz, R., Leiderer, P., and Scheer, E., "Optical transmission and laser structuring of silicon membranes," *Opt. Express* **17**(17), 15308–15317 (2009).
[46] Misawa, H. and Juodkazis, S., "Photophysics and photochemistry of a laser manipulated microparticle," *Prog. Polym. Sci.* **24**, 665–697 (1999).